Appl. Phys. B 76, 215–229 (2003)
DOI: 10.1007/s00340-002-1087-1

Applied Physics B
Lasers and Optics

W. LIU[1,✉]
O. KOSAREVA[2]
I.S. GOLUBTSOV[2]
A. IWASAKI[1]
A. BECKER[3,4]
V.P. KANDIDOV[2]
S.L. CHIN[1]

Femtosecond laser pulse filamentation versus optical breakdown in H_2O

[1] Département de Physique, de Génie Physique et d'Optique and Centre d'Optique, Photonique et Laser, Université Laval, Québec, QC, G1K 7P4, Canada
[2] International Laser Center, Physics Department, Moscow State University, Moscow, 119992, Russia
[3] Fakultät für Physik, Universität Bielefeld, Postfach 100 131, 33501 Bielefeld, Germany
[4] Max-Planck-Institut für Physik Komplexer Systeme, Nöthnitzer Strasse 38, 01187 Dresden, Germany

Received: 9 July 2002/Revised version: 15 November 2002
Published online: 19 March 2003 •

ABSTRACT The competition between femtosecond laser pulse induced optical breakdown and femtosecond laser pulse filamentation in condensed matter is studied both experimentally and numerically using water as an example. The coexistence of filamentation and breakdown is observed under tight focusing conditions. The development of the filamentation process from the creation of a single filament to the formation of many filaments at higher pulse energy is characterized systematically. In addition, strong deflection and modulation of the supercontinuum is observed. They manifest themselves at the beginning of the filamentation process, near the highly disordered plasma created by optical breakdown at the geometrical focus.

PACS 52.38.Hb; 42.65.Jx; 42.65.Tg; 33.80.Wz; 52.35.Mw

1 Introduction

The femtosecond laser has attracted much attention because of its wide potential applications. For example, in recent years, it has been reported that it is possible to write wave guides inside optical materials using an IR femtosecond laser [1–4]. Successfully writing such kinds of wave guides would impact upon the development of integrated optics. In contrast, the process during the interaction between the femtosecond laser and the material is not completely understood. Before, laser induced optical breakdown (OB) was thought to be the main contribution to the wave guide writing. But the breakdown plasma is so strong that it would induce real damage inside the material.

On the other hand, during the propagation of an ultrashort laser pulse in an optical medium, filamentation usually occurs, and has been observed in all kinds of optical materials, gases, liquids and solids (e.g. [5–13]). The filamentation is mainly the result of the balance between self-focusing of the laser pulse and the defocusing effect of the plasma generated at high intensities in the self-focal region. This plasma forms as a consequence of multiphoton/tunnel ionization (in gases) or multiphoton excitation of electrons from the valence to the conduction bands (in condensed matter). The filamentation process is accompanied by a broadening of the laser spectrum, as well as conical emission due to self-phase modulation and self-steepening [14, 15]. The spectrum can extend from the near infrared to the visible and is called the supercontinuum (SC) [16] or white light laser [17]. Due to its wide range of possible applications [18], the phenomenon has attracted much attention during recent years (e.g. [9, 12, 19–22]). Previous work has shown that in gases the plasma density needed to balance the self-focusing is much lower than the material density [23]. Later in this paper the simulation also gives the same result for water as an example of condensed matter. Once the balance is achieved, the maximum intensity inside the filaments becomes constant [13, 24, 25]. In condensed matter only a weak plasma is required to change the refractive index, but such a plasma is also necessary to avoid real damage [3, 4]. So filamentation has been thought to be a way to write wave guides and seems to produce better quality than using breakdown [3, 4]. Thus it is necessary to clarify the formation conditions of filamentation and breakdown.

In this article we will show that not only breakdown, but also filamentation, may occur in water under conditions similar to those for writing wave guides in glasses. It is possible to pass from filamentation without breakdown, through filamentation with breakdown, to breakdown without filamentation by changing the focal length and input energy.

2 Experiments

The experimental set-up is schematically illustrated in Fig. 1. The laser pulses were generated by a chirped-pulse-amplification (CPA) Ti:sapphire laser system, which includes a Ti:sapphire oscillator (Spectra Physics Maitai, 300 mW, 80 MHz), followed by a CPA regenerative amplifier (Spectra Physics Spitfire), at 1 kHz repetition rate, and a compressor. The generated laser pulses were centered at $\lambda_0 = 810$ nm with a 45 fs (FWMH) pulse duration and a beam diameter of $d = 5$ mm ($1/e^2$). The input pulse energy was controlled by a half-wave plate, which was located before the compressor. The laser pulse was focused by a microscope objective into a glass water cell. A series of microscope objectives (see Table 1) was used to vary the focal length in our experiment. Table 1 also shows the ratio $F = f/d$ of the focal length f and the input beam diameter d. The water cell was 2 cm in length and 2 cm in diameter, while the windows of the

✉ Fax: +1-418/6562-623, E-mail: wliu@phy.ulaval.ca

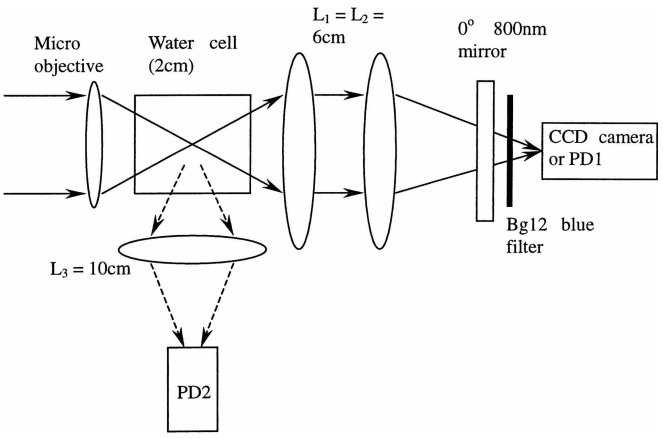

FIGURE 1 The experimental setup

Microscope objective	1×	2.5×	4×	6.3×	10×	16×
Focal length f (mm)	73.5	43.1	30.8	22.5	16.9	10.8
$F = f/d$	14.7	8.6	6.2	4.5	3.4	2.2

TABLE 1 Focal lengths of the microscope objectives used in the experiment

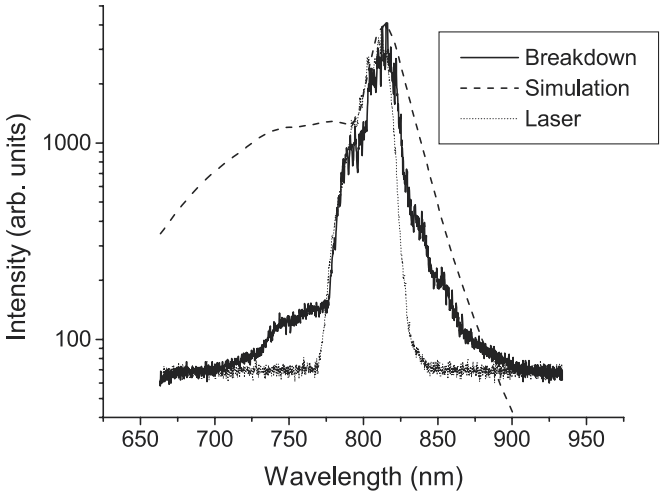

FIGURE 3 The laser spectrum with (*solid line*) and without (*dotted line*) optical breakdown measured at an input pulse energy of 4 μJ for a 16× micro objective ($f = 10.8$ mm, $F = 2.2$). *Dashed line*: the simulated spectrum obtained for an input pulse energy of 3 μJ and focal length $f = 16.9$ mm ($F = 3.4$). The simulated spectrum is integrated over the whole transverse aperture. Propagation distance $z = -0.035$ mm from the position of the geometrical focus in the water cell

cell were 1 mm thick. The geometrical focus was located at the center of the cell.

Two detection systems were used to monitor the signals from the geometrical focus, one in the forward direction and one from the side. The breakdown plasma causes a strong scattering of the laser light from the geometrical focal region. We therefore imaged the geometrical focus from the side using a $f = 10$ cm lens onto a photodiode (PD2) to observe the scattered light. We carefully checked and found that the light scattered by the plasma inside the filaments was too weak to be recorded by PD2. Thus the PD2 signal only manifested the appearance of OB. Independently, the appearance of optical breakdown was also determined by an infrared viewer, which detected strongly scattered IR laser light when breakdown occurred. When there was only filamentation, nothing could be seen through the viewer. (Incidentally, this latter observation also indicates that the electron density inside the filament is much weaker than that inside a breakdown plasma.) The results of both observations were in agreement: whenever we saw scattered laser light at the geometrical focus through the infrared viewer, we also observed the signal from the PD2 via the oscilloscope.

We firstly measured the thresholds for filamentation and OB for the whole series of microscope objectives. In the forward direction we used a white screen to determine the appearance of filamentation. Note that filamentation is accompanied by SC, which can easily be seen as a white light spot on the screen by eyes [13, 26]. We increased the laser energy from the minimum upwards. The thresholds are plotted in Fig. 2 as a function of the focal length of the micro-

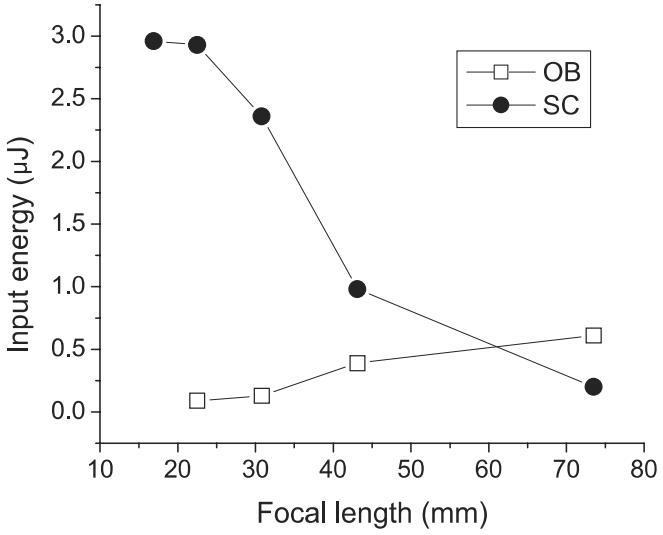

FIGURE 2 Threshold energies for supercontinuum generation (SC, *filled circles*) and optical breakdown (OB, *open squares*)

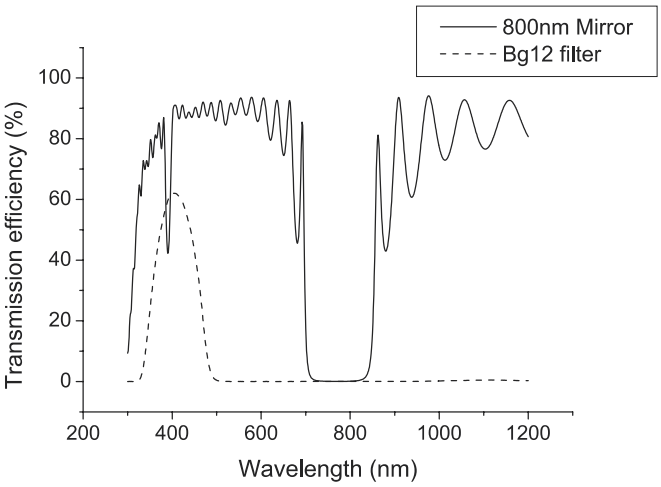

FIGURE 4 The transmission spectra of the 800 nm mirror (*solid line*) and the Bg12 filter (*dashed line*)

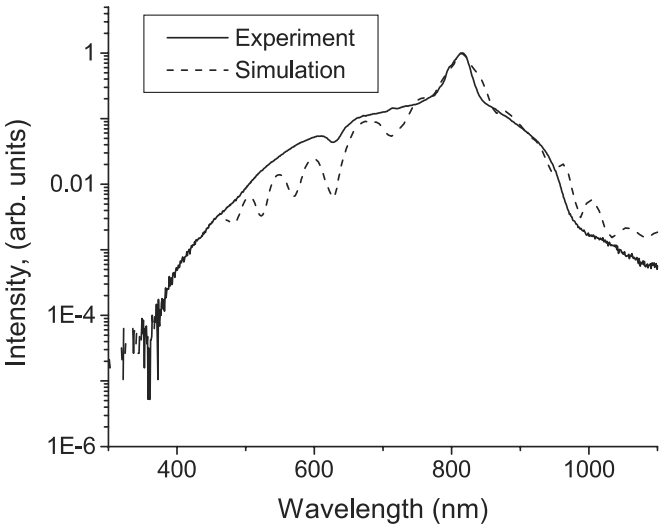

FIGURE 5 Typical supercontinuum spectrum in water. Experiment (*solid line*), simulations (*dashed line*). In the simulations the input pulse energy was 3 μJ and the focal length was $f = 73.5$ mm ($F = 14.7$). The spectrum is integrated over the whole transverse aperture. Propagation distance $z = -0.66$ mm from the position of the geometrical focus in the water cell

scope objectives (SC: filled circles, OB: open squares). For the shortest focal lengths (10.8 and 16.9 mm), the threshold for OB was found to be below the minimum input laser energy of 0.04 μJ, and so the results for these objectives are not presented in Fig. 2. Also, not shown in Fig. 2 is the point for SC at $f = 10.8$ mm, since we did not observe SC generation up to the maximum input laser energy of 4 μJ. We restricted ourselves to this upper limit of 4 μJ in view of possible damage of the microscope objectives at high laser energies. When only OB set in without SC, we measured the output laser spectrum in the forward direction by using an Ocean Optics S2000 fiber spectrometer. The spectrum is shown in Fig. 3 (solid line) together with the input laser spectrum (dotted line). The spectrum with OB is broader than the input laser spectrum.

Furthermore, in the forward direction, instead of using the screen, the light was collected by two lenses (both with $f = 6$ cm) onto a detector (c.f. Fig. 1), which was either a photodiode (PD1) or a large detection area CCD camera (8.8 mm × 6.6 mm). The video signal of the CCD camera was recorded by a computer via a LPA-300 capture card, while the signal of the photodiode was observed on an oscilloscope. A Bg12 blue filter and a 0° incident angle dielectric mirror (with ∼ 100% reflectivity around 800 nm) were used in front of the PD1 or the CCD camera. The transmission spectra of both the optical elements are shown in Fig. 4. The blue filter has a transmission spectrum from 315 nm to 525 nm with a maximum efficiency at 400 nm and the maximum reflection (up to 99.95%) of the mirror was near 800 nm. A typical supercontinuum (SC) spectrum is shown in Fig. 5 as a solid line. It extends from about 365 nm to above 1000 nm and is much broader than the optical breakdown spectrum (Fig. 3, solid line). Due to intensity clamping inside the filaments, the broadening of the SC spectrum was constant for laser input powers above the threshold power for filamentation [13]. Comparison of the spectra in Fig. 3 and Fig. 5 with the transmission spectra in Fig. 4 shows that the introduction of these optical elements is sufficient to fil-

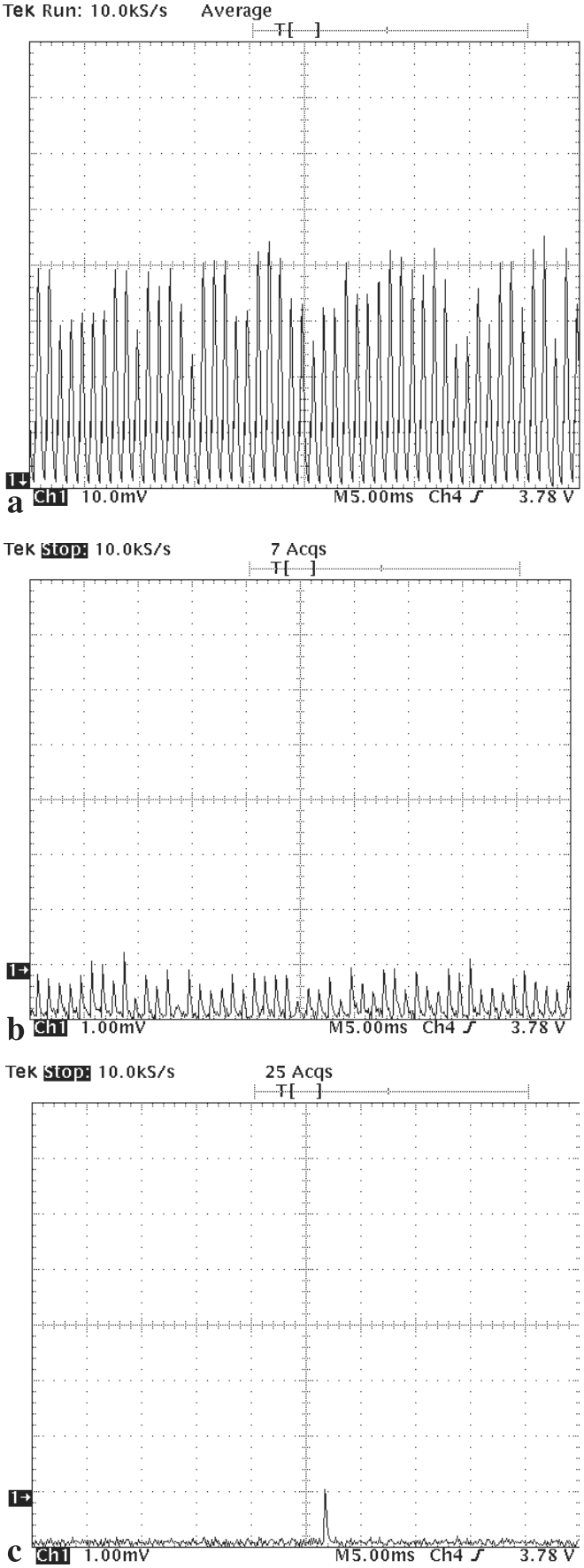

FIGURE 6 Oscilloscope signal at an input energy of 3 μJ for different micro objectives, namely **a** 1×, **b** 4×, and **c** 10×

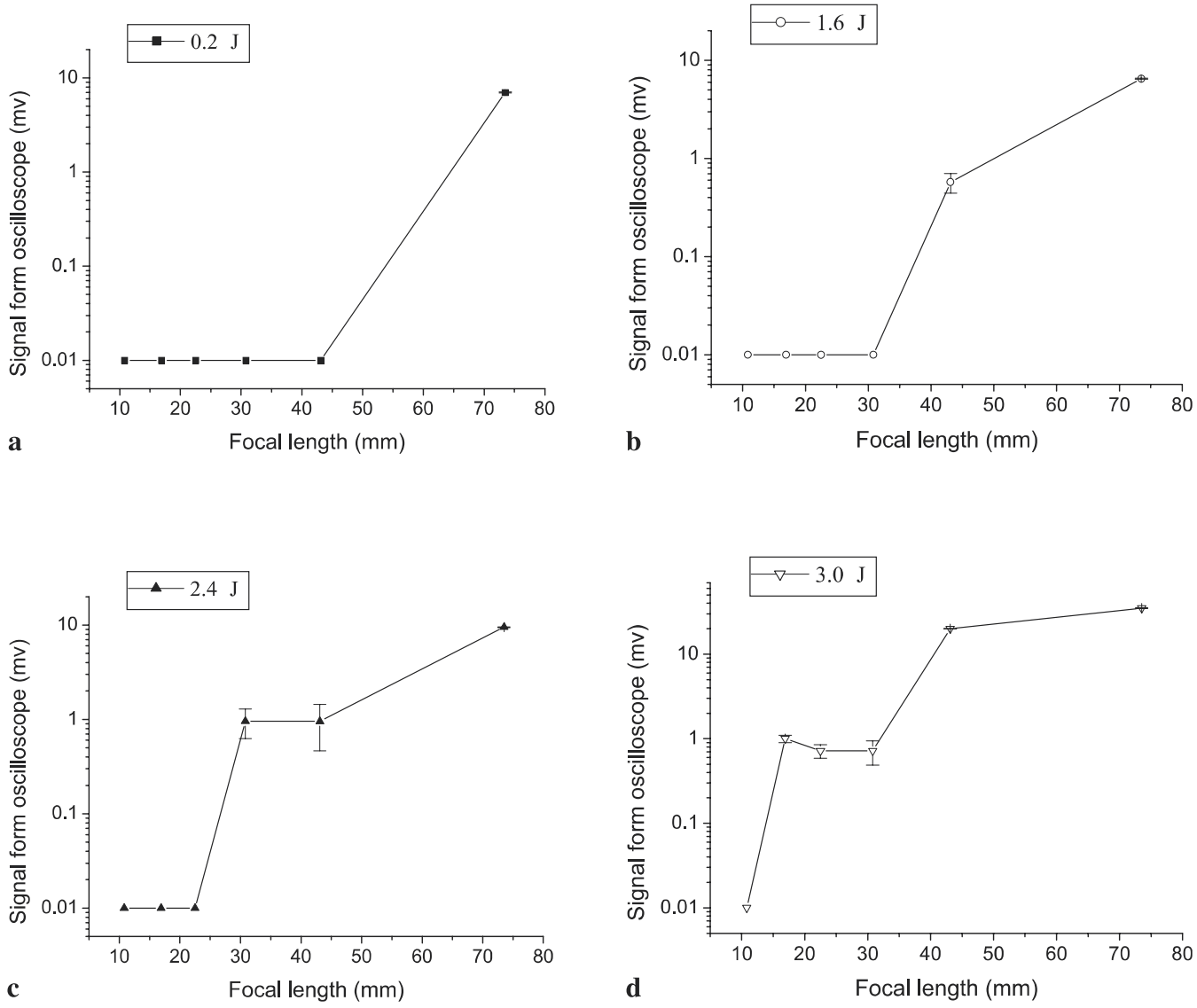

FIGURE 7 Averaged energy in the supercontinuum spectrum as a function of the focal length, measured via the oscilloscope, at various input energies: **a** 0.2 μJ, **b** 1.6 μJ, **c** 2.4 μJ, and **d** 3.0 μJ

ter both the strong laser spectrum around 800 nm and the OB spectrum.

We present in Fig. 6 the signal detected with the photodiode PD1 (c.f. Fig. 1) and recorded by an oscilloscope at an input energy of 3.0 μJ for different microscope objectives, namely (a) $f = 73.5\,\text{mm}\,(1\times)$, (b) $f = 30.8\,\text{mm}\,(4\times)$ and (c) $f = 16.9\,\text{mm}\,(10\times)$. The signals differed for all the three cases investigated: for the longest focal length (panel a) an average signal of 30 mV was observed, while the signal remained at about 1 mV for both the shorter focal lengths (panel b and c). On the other hand, the frequency at which the signal appeared was equal to 1 kHz, corresponding to the repetition rate of the laser, for the $1\times$ and $4\times$ microscope objectives, but it dropped to less than 20 Hz for the $10\times$ microscope objective. In addition, during the experiment with the $10\times$ microscope objective, we observed by eye a random appearance of the SC white light beam at cone angles of up to ± 40 degrees with respect to the laser propagation direction. We characterize this observation as a jumping or moving white light behavior. When the SC occurs randomly at different angles, it will hit the small opening of the photodiode very rarely, as observed on the oscilloscope (Fig. 6c). We further observed that the jumping behavior of the white light beam was accompanied by a random distribution of the color components inside the SC spot. Since the CCD camera works at 25 frames per second and can be video triggered, we used it to record all the moving white light shots. During a period of 5 minutes 54 shots were recorded, and 253 shots were recorded in 30 minutes.

In order to further study the energy distribution in the SC spectrum, we varied the input energy for each microscope objective. In Fig. 7 the averaged signal detected by the photodiode (PD1) at the oscilloscope is shown as a function of the focal length of the microscope objective at input energies per pulse of (a) 0.20 μJ, (b) 1.6 μJ, (c) 2.4 μJ and (d) 3 μJ. Roughly three levels for the signal were observed: 0 mV, 1 mV and 10–30 mV. For a convenient log-scale plot, we used 0.01 mV to denote 0 mV in Fig. 7. The largest signals (and

hence, energies) were detected for the longest focal lengths at all input energies. For an input energy of 0.2 μJ, as the focal length was shortened, the signal dropped directly below the detection limit (panel a), while for all the other input energies the signal first dropped to the 1 mV level, maintained this level for a few shorter focal lengths, before it finally dropped below the detection limit.

3 Discussion

3.1 *Self-focusing, filamentation, supercontinuum generation and optical breakdown*

We briefly recall some features of the two nonlinear processes, namely filamentation and optical breakdown. The filamentation process is initiated by self-focusing of the laser pulse, which occurs when the input laser power Pexceeds the critical power P_{crit}, given by [27]

$$P_{\mathrm{crit}} = \frac{3.77\lambda^2}{8\pi n_0 n_2} \ , \tag{1}$$

where λ is the laser wavelength, and n_0 and n_2 characterize the intensity dependent refractive index $n = n_0 + n_2 I$. The self-focus has been found to be approximately equal to the starting point of the filament [11]. Without external focusing a parallel beam with a Gaussian beam profile will self-focus at [27]

$$z_{\mathrm{f}} = \frac{0.367ka^2}{\left\{\left[\left(\frac{P}{P_{\mathrm{crit}}}\right)^{1/2} - 0.852\right]^2 - 0.0219\right\}^{1/2}} \ . \tag{2}$$

Here ka^2 is the diffraction length, where k is the wave number and a is the radius at the $1/e^2$ level of the beam profile. In the case of external focusing, using a lens of focal length f, the position of the self-focus will change to [11]

$$z_{\mathrm{f}}' = \frac{z_{\mathrm{f}} f}{z_{\mathrm{f}} + f} \ , \tag{3}$$

where $z_f{}'$ is the distance behind the focusing lens. From (2) and (3) it can be seen that the position of the self-focus and, hence, the starting point of the filament will move from the geometrical focus towards the lens as the input laser power is increased above the critical power P_{crit}. $P_{\mathrm{crit}} = 4.2$ MW has been measured in water before [10]. The critical power is roughly equal to the supercontinuum threshold power [10], which coincides with our experimental result that $P_{\mathrm{crit}} = 4.4$ MW (0.2 μJ and 1× micro objective, Fig. 7a).

In addition, laser pulse propagation will be dominated by self-focusing only when the instantaneous power is above the critical power. Otherwise it will still mainly obey linear propagation dynamics, and thus will be geometrically focused if external focusing is applied. As in the present experiment, self-focusing can lead to such high intensities near the geometrical focus that optical breakdown occurs [28, 29]. OB is a cumulative process in time. It starts from multiphoton ionization or excitation, followed by inverse Bremstrahlung and cascade ionization, resulting in the generation of a strong plasma. Though optical breakdown of condensed media with ultrashort pulses is not well understood yet, its threshold intensity for a pulse duration on the order of 45 fs can be estimated as follows.

The number of free electrons N_{e} in water increases over the course of the avalanche ionization according to the following law:

$$\frac{\mathrm{d}N_{\mathrm{e}}}{\mathrm{d}t} = \nu_{\mathrm{i}} N_{\mathrm{e}}, \ N_{\mathrm{e}}(t) = N_{\mathrm{e}0} \exp\left(t\nu_{\mathrm{i}}\right) , \tag{4}$$

where $N_{\mathrm{e}0}$ is a background initial density and the ionization frequency ν_i is given by [30]

$$\nu_{\mathrm{i}} = \frac{1}{W_{\mathrm{g}}} \frac{e^2 E^2}{2m\left(\omega^2 + \nu_{\mathrm{c}}^2\right)} \nu_{\mathrm{c}} \ . \tag{5}$$

Here E is the electric field amplitude, ω is the laser central frequency, m and e are the electron mass and charge, respectively, W_g is the band gap energy and

$$\nu_{\mathrm{c}} = N_{\mathrm{a}} v_{\mathrm{e}} \sigma_{\mathrm{c}} \tag{6}$$

is the electron collision frequency expressed through the density of neutrals N_{a}, the root-mean-square electron velocity v_{e} and the electron collision cross section σ_{c}. The velocity v_{e} is proportional to the square root of the laser intensity $I = \frac{cn_0}{8\pi} |E|^2$. Thus, the avalanche ionization frequency (5) depends on the intensity according to $\nu_{\mathrm{i}} \sim I^{3/2}$, if $\nu_{\mathrm{c}} << \omega$.

There are several ways to define the threshold plasma density for optical breakdown. The authors of [31] suggest two possible definitions for the breakdown density in water. This density can be defined by the appearance of vapor bubbles in the water sample, the "bubble" endpoint, or by the appearance of visible emission, the "flash" endpoint. The former definition is usually used when studying ultrashort pulses with durations shorter than 10 ps. In this case the threshold breakdown density is $N_{\mathrm{e\,th}} \approx 10^{18}\,\mathrm{cm}^{-3}$. The latter definition is used for long pulses with durations on the order of a nanosecond. The threshold breakdown density is then $N_{\mathrm{e\,th}} \approx 10^{20}\,\mathrm{cm}^{-3}$ [31]. Another possible definition of the breakdown threshold density is the critical density of the plasma $N_{\mathrm{cr}} = \pi\, m\, c^2/(e^2\, \lambda_{\mathrm{w}}^2)$, where m and e are the electron mass and charge, respectively, and λ_{w} is the laser wavelength. This definition was used, for example, in [32] for studying breakdown in fused silica. Under our experimental conditions of 45 fs laser pulse propagation in water, the most appropriate definition of the breakdown density is $N_{\mathrm{e\,th}} \approx 10^{18}\,\mathrm{cm}^{-3}$, since breakdown was detected by the scattered IR light of the laser, and not by the visible emission, in the experiment.

The ionization frequency ν_{i} needed to cause the avalanche can be expressed as $\nu_{\mathrm{i}} = \ln\left(N_{\mathrm{e\,th}}/N_{\mathrm{e}0}\right)/t$ from (4). Taking the threshold density to be $N_{\mathrm{e\,th}} = 10^{18}\,\mathrm{cm}^{-3}$ and the background electron density in water as $N_{\mathrm{e}0} = 10^{15}\,\mathrm{cm}^{-3}$, we have $\nu_{\mathrm{i}} \approx 7/t$. For a time scale on the order of $t = 45$ fs, the ionization frequency should be $1.5 \times 10^{14}\,\mathrm{s}^{-1}$ to cause the avalanche. Considering the laser central wavelength as 810 nm; the band gap energy for water as $W_{\mathrm{g}} = 6.5$ eV, the density of neutrals as $N_{\mathrm{a}} = 3.3 \times 10^{22}\,\mathrm{cm}^{-3}$ and the cross section as $\sigma_{\mathrm{c}} = 10^{-15}\,\mathrm{cm}^2$ [30], we obtain the threshold breakdown intensity as $I_{\mathrm{th}} = 8.8 \times 10^{12}\,\mathrm{W/cm}^2$. We note, that the value of

$I_{\rm th}$ is not very sensitive to the ratio $N_{\rm e0}/N_{\rm e\,th}$. The decrease of the background density $N_{\rm e0}$ from $10^{15}\,{\rm cm}^{-3}$ to $10^{12}\,{\rm cm}^{-3}$, with the simultaneous increase of the threshold density $N_{\rm e\,th}$ from $10^{18}\,{\rm cm}^{-3}$ to the critical plasma density $10^{21}\,{\rm cm}^{-3}$, leads to a change in the intensity $I_{\rm th}$ from $8.8\times10^{12}\,{\rm W/cm}^2$ to $1.7\times10^{13}\,{\rm W/cm}^2$. Earlier calculations of the breakdown threshold intensity gave us $I_{\rm th}=5.4\sim5.6\times10^{12}\,{\rm W/cm}^2$ for a 100 fs pulse [33]. If we only take into account linear propagation in our experiments, the OB threshold intensity with $f=22.5$ mm is $1.2\times10^{13}\,{\rm W/cm}^2$, corresponding to an input energy of 0.09 μJ. This estimation is in reasonable agreement with our observations (Fig. 2).

Since the filamentation threshold is defined by the power and the OB threshold is defined by the intensity, the competition between optical breakdown and filamentation depends on the focusing geometry. Using a tight focusing geometry will favor OB, since the geometric convergence is strong enough to provide the intensity increase up to the breakdown threshold intensity. On the other hand, in the case of weak focusing, the intensity growth is mainly determined by the self-focusing. In this case the plasma is produced in the course of filament formation, as soon as the intensity reaches the ionization threshold intensity.

Due to the influence of nonlinear propagation, the OB threshold in Fig. 2 increases slightly with an increase of the focal length, but not as f^2 as would be expected for geometrical focusing. These results are in agreement with previous measurements in gas [26], where they were attributed to the strong distortion of the laser beam by self-focusing during the propagation of the pulse. On the other hand, in the case of weak focusing, the threshold power for OB in the geometrical focal region increases and can, in principle, exceed the critical power for self-focusing, filamentation and SC generation.

3.2 *Numerical simulations*

Our theoretical model for nonlinear propagation in water is based on the wave equation for the slowly varying envelope approximation coupled to the equation for the free-electron density. A similar system of equations was used earlier for a description of filamentation in air [14, 34], except that here we have included avalanche ionization and electron recombination into the electron density equation. Assuming propagation occurs along the z axis with the group velocity $v_{\rm g}$, the equation for the electric field envelope $E(r,z,t)$ is

$$2{\rm i}k\left(\frac{\partial E}{\partial z}+\frac{1}{v_{\rm g}}\frac{\partial E}{\partial t}\right)=\left(1-\frac{\rm i}{\omega}\frac{\partial}{\partial\tau}\right)^{-1}\Delta_\perp E-kk''_\omega\frac{\partial^2E}{\partial t^2}+\frac{2k^2}{n_0}\left(\left(1-\frac{\rm i}{\omega}\frac{\partial}{\partial\tau}\right)\Delta n_{\rm k}+\left(1+\frac{\rm i}{\omega}\frac{\partial}{\partial\tau}\right)\Delta n_{\rm p}\right)E-{\rm i}k\alpha E \qquad (7)$$

where the first term on the right-hand-side describes diffraction, and the second term describes group velocity dispersion. In the third term we take into account the nonlinearity of the medium and self-steepening of the pulse over the course of propagation. The last term on the right-hand-side of (7) describes the energy losses due to electron transitions to the conduction band; where $k=2\pi n_0/\lambda_0$ is the wavenumber, and ω is the laser central frequency. The operator $\frac{\rm i}{\omega}\frac{\partial}{\partial\tau}$ on the right-hand side of (7) is the result of taking into account higher order correction terms to the slowly varying envelope approximation. These correction terms allow one to describe the propagation of ultrashort pulses with durations on the order of one optical cycle [35]. In our case the pulse contains more than 16 optical cycles, but at the same time, the steep fronts require the inclusion of this operator into the propagation equation [14, 15].

Nonlinearity is described by the instantaneous Kerr contribution and the plasma contribution. The Kerr contribution $\Delta n_{\rm k}$ is given by

$$\Delta n_{\rm k}=\frac{1}{2}n_{\rm 2eff}\,|E|^2\,, \qquad (8)$$

where $n_{\rm 2eff}$ is defined through the experimentally obtained critical power for self-focusing in water (1): $n_{\rm 2eff}=\frac{3.77\lambda^2}{8\pi n_0\,P_{\rm crit}}\approx2\times10^{-16}\,{\rm cm}^2/{\rm W}$. Introduction of the effective value of the nonlinear coefficient n_2 allows us to take into account the noninstantaneous nonlinear response of water [36]. The plasma contribution $\Delta n_{\rm p}$ is given by

$$\Delta n_{\rm p}=\frac{1}{2}\left(\frac{{\omega_{\rm p}}^2}{\omega^2+{\nu_{\rm c}}^2}+{\rm i}\frac{\nu_{\rm c}}{\omega}\frac{{\omega_{\rm p}}^2}{\omega^2+{\nu_{\rm c}}^2}\right). \qquad (9)$$

Here $\omega_{\rm p}^2=\frac{4\pi e^2\,N_{\rm e}}{m}$ is the plasma frequency and $N_{\rm e}(r,z,t)$ is a free-electron density, the equation for which is [5, 30, 33]

$$\frac{\partial N_{\rm e}}{\partial t}=R\left(|E|^2\right)(N_{\rm a}-N_{\rm e})+\nu_{\rm i}N_{\rm e}-\beta N_{\rm e^2}. \qquad (10)$$

The avalanche ionization frequency $\nu_{\rm i}$ is given by (5) and the electron collision frequency $\nu_{\rm c}$ by (6). The optical-field-induced ionization rate $R\left(|E|^2\right)$, which depends on the light intensity, is calculated according to [37]. The radiative electron recombination coefficient is given by [30]:

$$\beta=\frac{8.75\times10^{-27}}{T^{9/2}}N_{\rm e}\,\left[{\rm cm}^3/{\rm s}\right], \qquad (11)$$

where T is the electron temperature in the laser-produced plasma in eV.

The pulse at the entrance to the water cell is Gaussian in space and time:

$$E\,(r,z=0,\tau)=E_{\rm in}\exp\left(-\tau^2/2{\tau_0}^2\right)\times\exp\left(-r^2/2a_0^2+{\rm i}kr^2/2R_{\rm f}\right), \qquad (12)$$

where $\tau=t-z/v_{\rm g}$, $2\tau_0=54$ fs corresponds to 45 fs FWHM, and a_0 is the beam radius. In the simulations we used the group velocity dispersion coefficient ${k_\omega}''\approx3\times10^{-28}\,{\rm s}^2/{\rm cm}$, calculated for $\lambda=810$ nm from the data on refractive index for different wavelengths presented in [38].

The geometry of propagation corresponds to that used in the measurements. The simulations started from the entrance to the water cell, where the radius a_0, the intensity $I_{\rm in}=\frac{cn_0}{8\pi}\,|E_{\rm in}|^2$, and the focal distance $R_{\rm f}$ used in (12) were recalculated from the actual beam diameter of 5 mm ($1/e^2$), the experimental peak power of the input pulse, and the geometrical focal distance f of the micro objective (see Table 1),

according to the formulas for linear diffraction of Gaussian beams (see, e.g., [39]). For these calculations the distance of linear propagation in air was the distance between the micro objective and the entrance to the water cell. The focal distance R_f used in the simulations (see (12)) was 1 cm with an accuracy of 0.2%. This is in agreement with the geometry of the experiment, where the geometrical focus was always located at the center of the 2 cm cell. We need to note that the glass window of the water cell does not influence the beam propagation significantly. It has been shown [40] for similar input parameters that laser beam filamentation and strong ionization within a 1 mm glass plate occurs only when the beam radius does not exceed 30 μm. In the present experiment, the minimum beam radius at the entrance of the window was 170 μm and, hence, far above this limit. The influence of the glass window is therefore negligible. Furthermore, the group velocity dispersion in air was not taken into account, since the distance between the compressor and water cell was about 1.5 m, while the dispersion length is around 50 m for 45 fs pulses in air. This value is an order of magnitude larger than the propagation distance before the water cell.

The results of our numerical simulations are summarized in Figs. 8–13. The effect of self-steepening on the pulse propagation was taken into account only in the case of focusing with the 16.9 mm focal length. In the simulations with longer geometrical focusing lengths of 43.1 and 73.5 mm, we did not take into account the terms with the operator $\frac{i}{\omega}\frac{\partial}{\partial\tau}$ in (7), due to dramatic steepening of the pulse fronts in water, which could not be adequately reproduced on the numerical grid. This steepening effect increases with an increase of the self-focusing effect rather than with geometrical focusing. Therefore, self-steepening becomes more pronounced with a longer geometrical focusing distance and larger pulse energy. At the same time, intensity spikes resulting from self-steepening are localized in space and time and have nearly no effect on the overall intensity, fluence, electron density distributions and

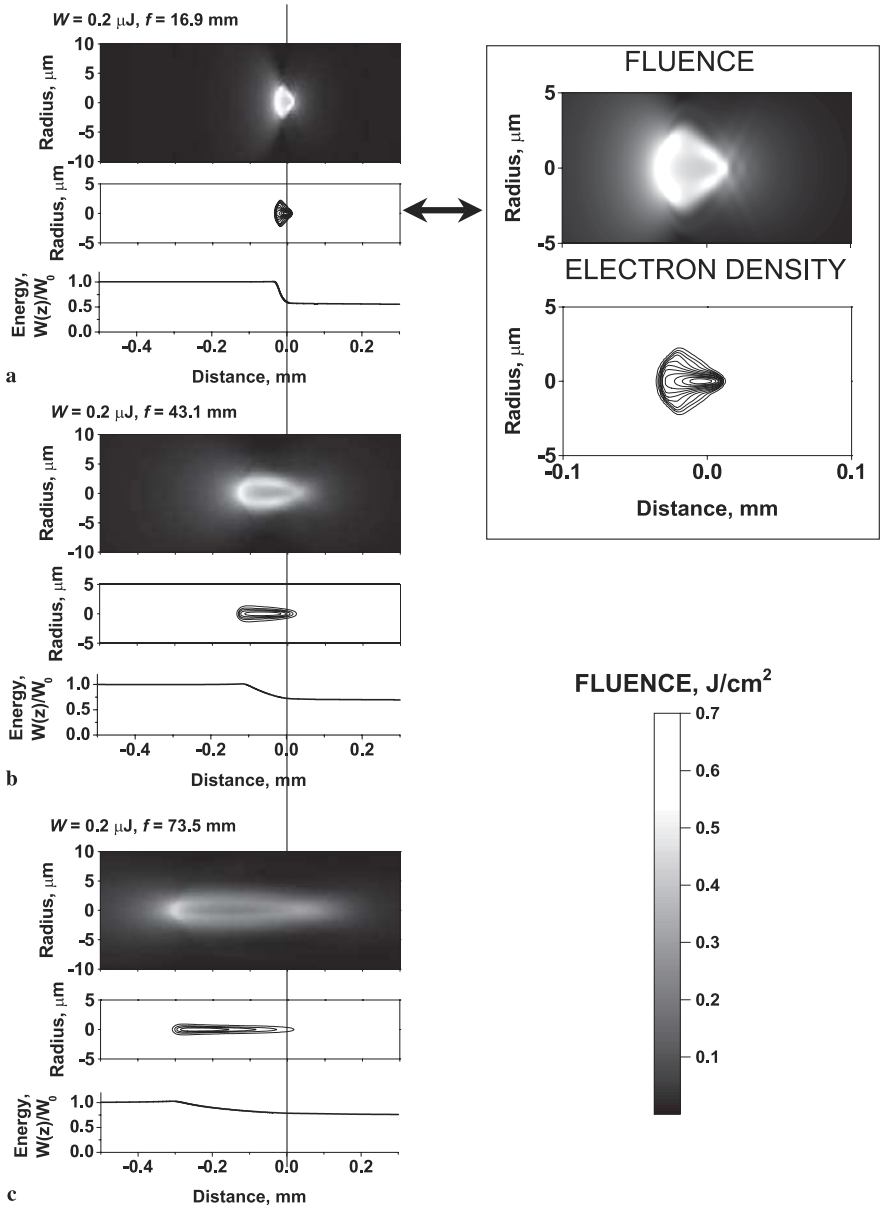

FIGURE 8 The simulated evolution of the fluence distribution, electron density distribution and the total pulse energy in the water cell. For **a–c**, the upper plot is the fluence distribution, the middle plot is the electron density distribution, and the lower plot is the change of the total pulse energy $W(z)/W$. The horizontal axis coincides with the propagation axis z. The position of the geometrical focus ($z = 0.0$ mm) is indicated by the *vertical solid line*. The initial pulse energy is $W = 0.2$ μJ and $P_{peak}/P_{crit} = 1.01$. The interval between the electron density contours in (a)–(c) is $\Delta N_e = 0.002\, N_a$. **a** The focal length of the lens is $f = 16.9$ mm ($F = 3.4$), the maximum electron density is $N_{e\,max} = 0.023\, N_a$. **b** $f = 43.1$ mm ($F = 8.6$), $N_{e\,max} = 0.010\, N_a$. **c** $f = 73.5$ mm ($F = 14.7$), $N_{e\,max} = 0.008\, N_a$

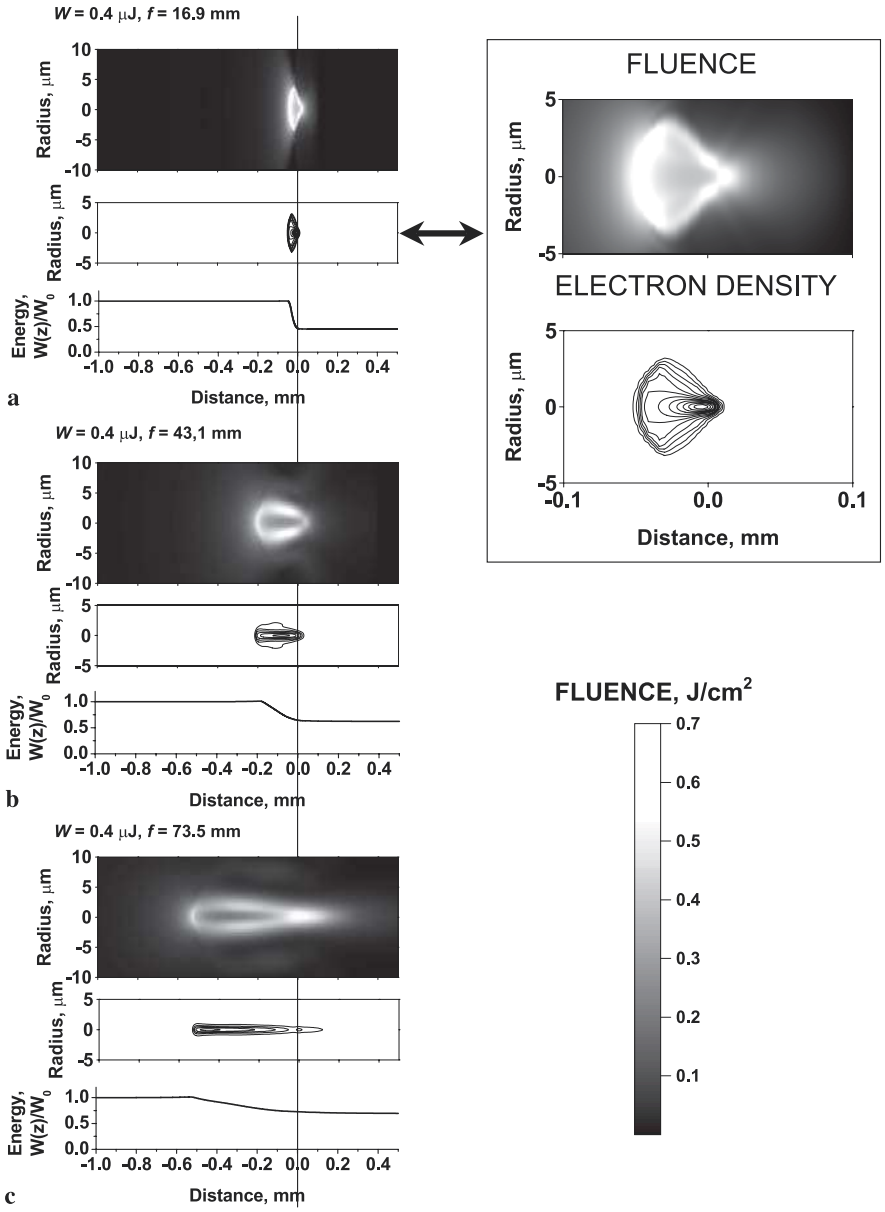

FIGURE 9 Simulation results similar to those in Fig. 8 for $W = 0.4\,\mu\text{J}$, $P_{\text{peak}}/P_{\text{crit}} \approx 2$. The electron density maxima are **a** $N_{\text{e}\,max} = 0.024\,N_{\text{a}}$, **b** $N_{\text{e}\,max} = 0.011\,N_{\text{a}}$, and **c** $N_{\text{e}\,max} = 0.010\,N_{\text{a}}$

dependence of the pulse energy on the propagation distance. The latter fact is in agreement with the simulation results presented in [14].

In Figs. 8–10, for different focal distances, the upper plot in each panel shows the change of the fluence distribution with distance, the middle plot shows the change of the electron density with distance and the lower plot shows the change of the pulse energy $W(z)/W$, where W is the corresponding input pulse energy. Further on, when describing the simulation results and comparing them with the experiment, we will indicate both the energy of the pulse and the corresponding ratio of the initial pulse peak power P_{peak} to the critical power for self-focusing in water P_{crit} . In addition to the geometrical focal length f we will indicate the ratio $\text{F} = f/d$.

The initial pulse energies and the ratios $P_{\text{peak}}/P_{\text{crit}}$ were 0.2 μJ (Fig. 8, $P_{\text{peak}}/P_{\text{crit}} = 1.01$), 0.4 μJ (Fig. 9, $P_{\text{peak}}/P_{\text{crit}} \approx 2$) and 3 μJ (Fig. 10, $P_{\text{peak}}/P_{\text{crit}} \approx 15$). The horizontal axis shows the position along the water cell. The geometrical focal position is located at $z = 0$ and is indicated by the solid vertical line. Note the different horizontal axis scales in Figs. 8–10. The insets demonstrate the magnified fluence and electron density distributions for $f = 16.9$ mm (panels a). The geometrical focal distances f and the corresponding ratios $F = f/d$ were $f = 16.9$ mm ($F = 3.4$), $f = 43.1$ mm ($F = 8.6$), and $f = 73.5$ mm ($F = 14.7$). At the beginning of the water cell the propagation of the pulse is mainly defined by the geometrical focusing. As the pulse approaches the geometrical focus, self-focusing starts to contribute to the pulse transformation. The fluence distribution in the $\{r, z\}$ plane has a sickle-shaped structure with the first maximum located at the nonlinear focal position. In accordance with (2) and (3), this maximum approaches the geometrical focus with a decrease in the focal length of the lens for a constant energy (compare plots (a), (b), and (c) in Figs. 8–10) or with a decrease in the energy for a constant focal length (compare, e.g., plots in Figs. 8c, 9c and 10c). The nonlinear focal position $z = z_{\text{f}}{}''(= z_{\text{f}}{}' - f)$ indicates the start of the area with large values of the fluence. Further on, we will refer to this area with $z > z_{\text{f}}{}''$ as the filament.

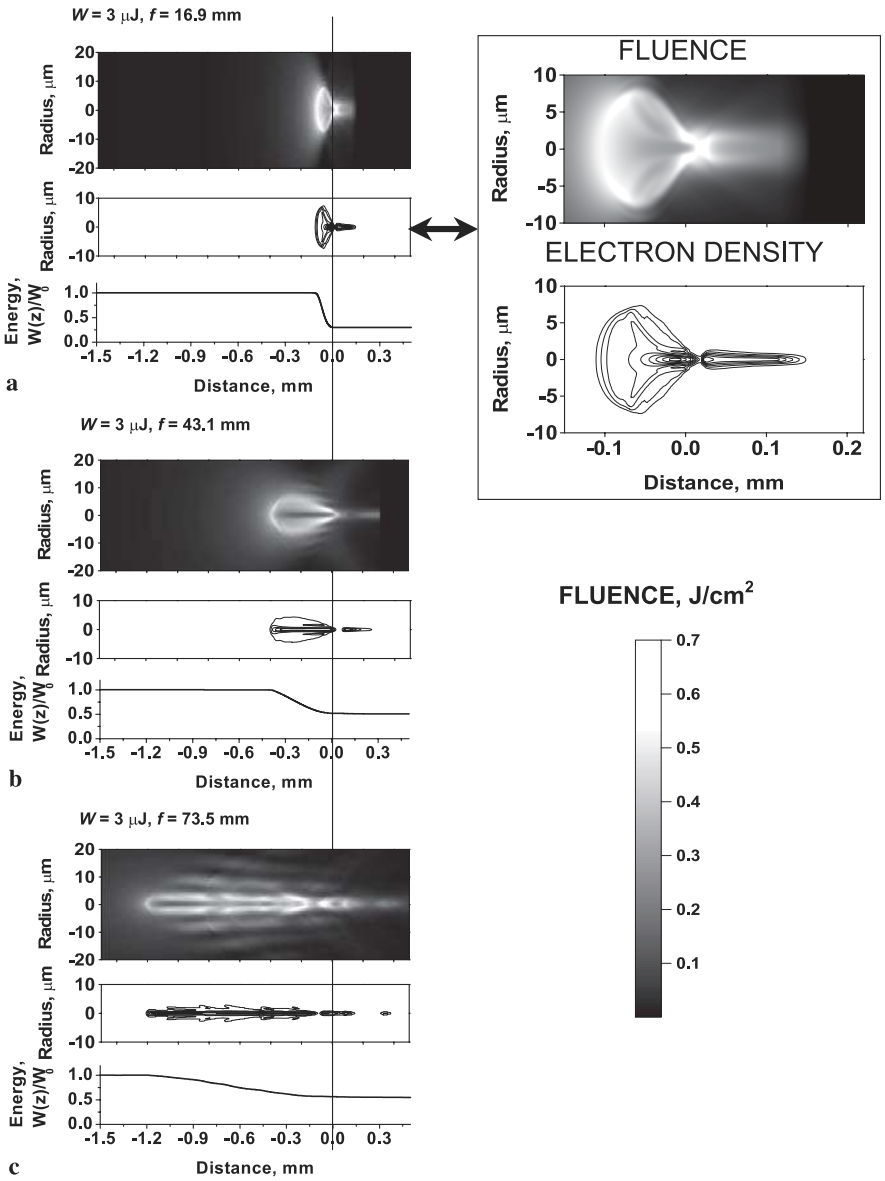

FIGURE 10 Simulation results similar to those in Fig. 8 for $W = 3\,\mu$J, $P_{\rm peak}/P_{\rm crit} \approx 15$. The electron density maxima are **a** $N_{e\,max} = 0.020\,N_a$, **b** $N_{e\,max} = 0.011\,N_a$, and **c** $N_{e\,max} = 0.012\,N_a$. The results for $f = 16.9$ mm were obtained with self-steepening in (7) taken into consideration

In the close vicinity of the nonlinear focal position $z = z_f''$, the peak intensity of the pulse grows rapidly and reaches the breakdown threshold intensity $I_{\rm th} \approx 10^{13}$ W/cm^2. The free electrons due to the laser-produced plasma are shown by the equal-density contours in Figs. 8–10. In all plots the minimum contour corresponds to the level 0.001 of the density of neutrals N_a and the interval between the contours is $\Delta N_e = 0.002\,N_a$. In the case of a short focal length lens with $f = 16.9$ mm (Figs. 8a–10a, $F = 3.4$), the major contribution to the pulse contraction is geometrical focusing. The separation between the nonlinear focus position z_f'' and the geometrical focal position $z = 0$ is small: $|z_f''| = 0.03 \sim 0.1$ mm. The plasma formation is governed by the geometrical convergence of the whole beam. The maximum transverse size of the breakdown region strongly depends on the input pulse energy. Its value, defined at the level of 0.001 of the initial density of neutrals N_a, is 4.4 μm for $W = 0.2\,\mu$J (inset of Fig. 8a, $P_{\rm peak}/P_{\rm crit} = 1.01$), 6.4 μm for $W = 0.4\,\mu$J (inset of Fig. 9a, $P_{\rm peak}/P_{\rm crit} \approx 2$) and 14 μm for $W = 3\,\mu$J (inset of Fig. 10a, $P_{\rm peak}/P_{\rm crit} \approx 15$). These maximum transverse sizes are achieved at $z = -0.02$ mm, at $z = -0.03$ mm and at $z = -0.05$ mm, respectively. At the same time the largest electron density value for $f = 16.9$ mm ($F = 3.4$) is nearly the same for all energies ($\approx 0.02\,N_a$). It is attained right before the geometrical focus at $z \approx -0.003$ mm.

In the case of longer focal length lenses with $f = 43.1$ mm ($F = 8.6$) and $f = 73.5$ mm ($F = 14.7$) (Figs. 8–10b,c), where self-focusing essentially contributes to the spatio-temporal contraction of the pulse, the separation between the nonlinear focus position $z = z_f''$ and the geometrical focal position $z = 0$ increases in comparison to the $f = 16.9$ mm ($F = 3.4$) focal length. The transverse size of the fluence and the plasma is smaller and remains more stable along the propagation axis for $z > z_f''$. This is well pronounced for the case of $f = 73.5$ mm ($F = 14.7$) and larger, where the elongated plasma channel is formed along the filament. The maximum transverse size of the plasma, defined at the level of $10^{-3}\,N_a$, is 1.8 μm for $W = 0.2\,\mu$J (Fig. 8c, $P_{\rm peak}/P_{\rm crit} = 1.01$), and 2 μm for $W = 0.4\,\mu$J (Fig. 9c, $P_{\rm peak}/P_{\rm crit} \approx 2$).

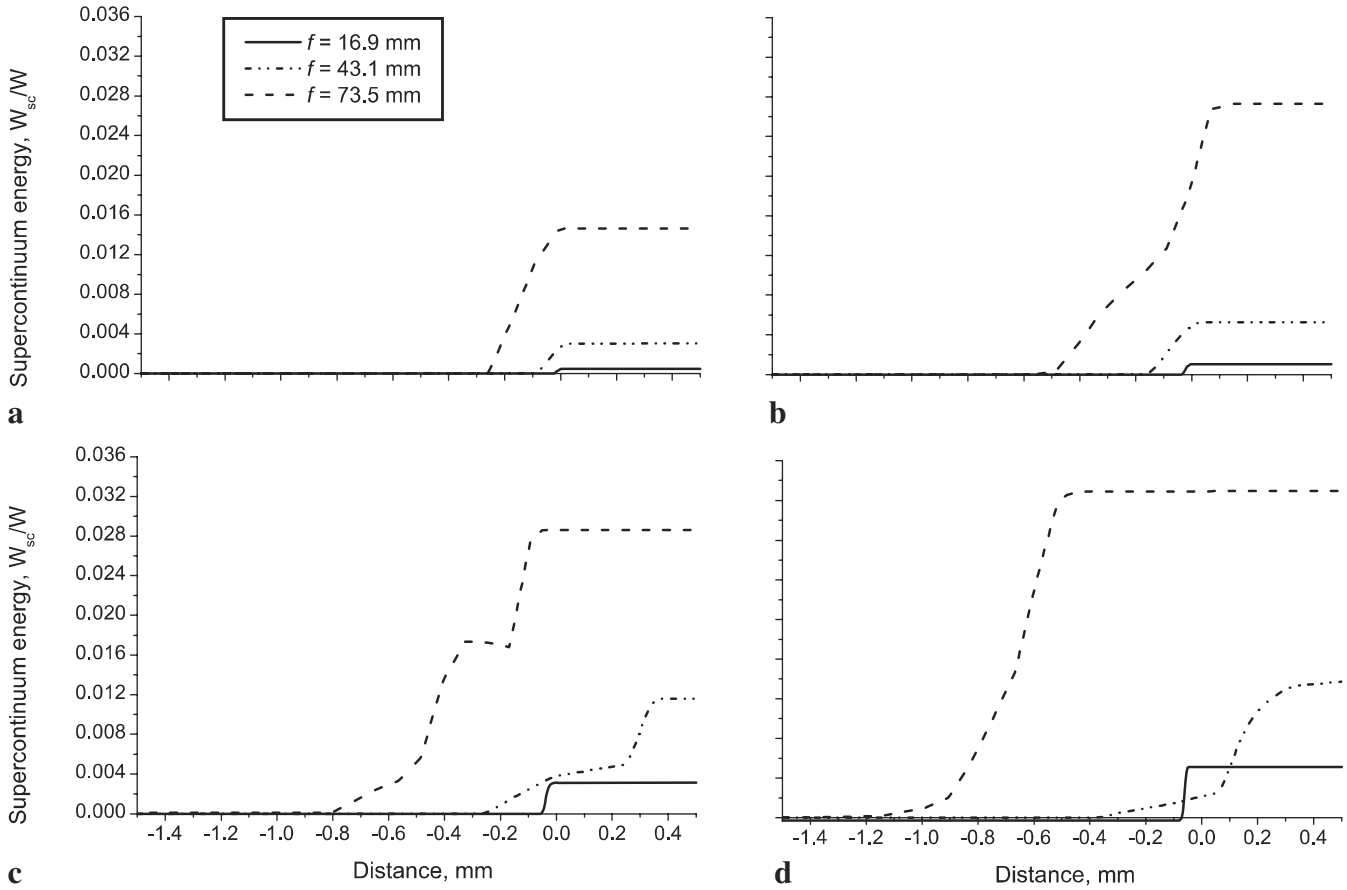

FIGURE 11 The simulated growth of the supercontinuum energy with propagation distance inside the water cell. The position of the geometrical focus is at $z = 0.0$ mm. For the calculations of the supercontinuum energy we 'filtered' all the radiation with $\lambda > 600$ nm. The *solid curve* corresponds to the $f = 16.9$ mm focal distance ($F = 3.4$), the *dash-dotted curve* corresponds to the $f = 43.1$ mm focal distance ($F = 8.6$), and the *dashed curve* corresponds to the $f = 73.5$ mm focal distance ($F = 14.7$). The initial pulse energies are: **a** 0.2 μJ, $P_{\text{peak}}/P_{\text{crit}} = 1.01$; **b** 0.4 μJ, $P_{\text{peak}}/P_{\text{crit}} \approx 2$; **c** 1 μJ, $P_{\text{peak}}/P_{\text{crit}} \approx 5$; **d** 3 μJ, $P_{\text{peak}}/P_{\text{crit}} \approx 15$. The results for $W = 3$ μJ, $f = 16.9$ mm were obtained with self-steepening in (7) taken into consideration

For an energy of $W = 3$ μJ (Fig. 10c, $P_{\text{peak}}/P_{\text{crit}} \approx 15$) the transverse size of the plasma increases up to 5.8 μm due to the ionization in the rings surrounding the filament. The maximum values of the electron density for $f = 73.5$ mm are achieved at $z = -0.28$ mm (Fig. 8c), at $z = -0.5$ mm (Fig. 9c) and at $z = -0.7$ mm (Fig. 10c). The electron density maximum decreases with an increase in the focal length and has values in the range $0.009 \sim 0.012\, N_{\text{a}}$ (Figs. 8–10c) for $f = 73.5$ mm, which is less than half the value in the case of the 16.9 mm geometrical focal distance.

The change of the fluence and the corresponding plasma distribution with a change in the focal length of the lens demonstrates the joint manifestation of filamentation and optical breakdown for different geometries of the experiment. Tight focusing leads to large transverse and small longitudinal sizes of the fluence and the plasma in combination with high values of the maximum electron density. On the contrary, a weak focusing leads to a small transverse, but a large longitudinal size of the fluence and the plasma, i.e. filamentation is more pronounced. At the same time, the values of the maximum plasma density are lower.

Plasma production and heating lead to strong energy loss (Figs. 8–10, lower plots in each series (a)–(c)). Only 30% of the input pulse energy remains after the geometrical focus for the case of a 3 μJ ($P_{\text{peak}}/P_{\text{crit}} \approx 15$) pulse and a focal length of $f = 16.9$ mm (Fig. 10a, $F = 3.4$). At the same time 50% and 54% of the input energy remains after focusing with the longer geometrical focal distances $f = 43.1$ mm and $f = 73.5$ mm, respectively (Fig. 10b,c, $F = 8.6$ and $F = 14.7$, respectively). With a decrease in the input pulse energy, the energy loss also decreases. In a 0.2 μJ pulse ($P_{\text{peak}}/P_{\text{crit}} = 1.01$) 63% of the input pulse energy remains after tight focusing with $f = 16.9$ mm ($F = 3.4$), and 75% of the input energy remains after weaker focusing with $f = 73.1$ mm ($F = 14.7$). For all input pulse energies and geometrical focal distances, the losses take place for propagation distances in the interval $z_{\text{f}}'' < z < 0$. The distance $|z_{\text{f}}''|$ decreases with a decrease in the geometrical focal distance according to (3). Therefore, the tighter the geometrical focusing, the larger the gradient of the energy loss in the breakdown plasma.

When the peak power of the input pulse is much larger than the critical power for self-focusing in water, there is still enough power for self-contraction after a large part of the input energy has been lost. In our simulations this is the case for a 3 μJ input pulse, for which $P_{\text{peak}}/P_{\text{crit}} \approx 15$. Behind the geometrical focus the "recovered" filament is created (Fig. 10a–c, upper plots, $z > 0$). In the recovered filament, plasma is also generated (Fig. 10a–c, middle plots). The extension of the filament behind the geometrical focus is similar to the refocusing phenomenon

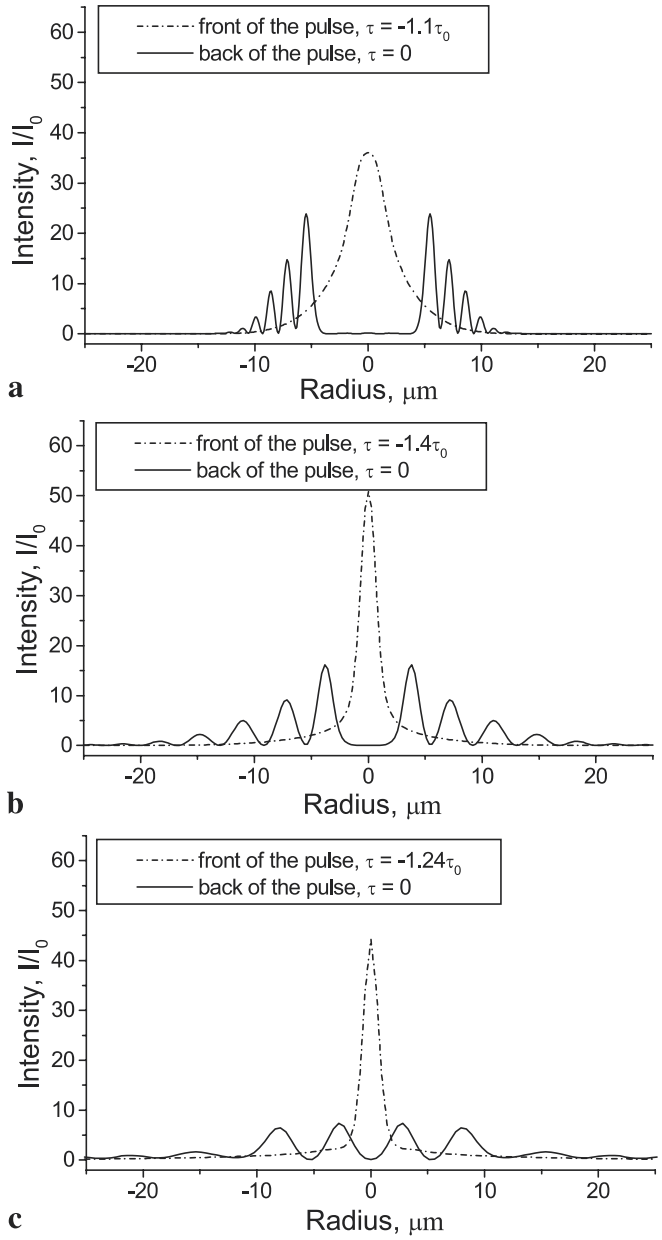

FIGURE 12 The simulated transverse intensity distributions in the vicinity of the geometrical focus. For the panels **a–c** the *dash-dotted line* is the intensity in the front of the pulse and the *solid line* is the intensity at the back of the pulse. The position of the geometrical focus is at $z = 0.0$ mm and $I_0 = 10^{12}$ W/cm^2. **a** $f = 16.9$ mm, $F = 3.4$, $z = -0.05$ mm; **b** $f = 43.1$ mm, $F = 8.6$, $z = -0.2$ mm; **c** $f = 73.5$ mm, $F = 14.7$, $z = -1.0$ mm

observed and simulated for the long light filaments in air [41–43].

The frequency spectra of the pulses were calculated at each spatial position (z, r) inside the water cell. The simulated spectra obtained above the threshold for supercontinuum generation have a typical distribution shown in Fig. 5 (dashed line) and are in good qualitative agreement with the experimentally obtained spectra (Fig. 5, solid line). If the combination of the input pulse energy and the focal length is such that we are below the threshold for supercontinuum generation, less spectral broadening is observed in both the experiment and simulations (Fig. 3). Larger broadening of the simulated spectra (compare dashed and solid lines in Fig. 3) may be accounted for by the fact that white light was strongly deflected from the forward direction for focal lengths with $f \leq 16.9$ mm in the experiment, and, therefore, part of the supercontinuum energy might not have been detected by the spectrometer.

In order to compare the simulated conversion efficiency of the radiation to supercontinuum with the experiment, we have calculated the energy W_{sc} contained in the blue wing of the transmitted pulse spectrum:

$$W_{sc}(z) = 2\pi \int_0^{\infty} r\mathrm{d}r \int_{\lambda_{min}}^{\lambda_{max}} S(\lambda, r, z)\mathrm{d}\lambda, \tag{13}$$

where $S(\lambda, r, z)$ is the spectral intensity of the pulse at a certain position r inside the aperture and the wavelength λ is measured in nanometers. The upper limit of the integration was taken as $\lambda_{max} = 600$ nm. Note that in the experiment the blue wing was limited by a smaller wavelength of 500 nm defined by the blue filter (Fig. 4). We have chosen 600 nm as the upper limit because the shortest wavelength λ_{min} reproduced in our simulations was 470 nm, while in the experiment the supercontinuum extended up to 350 nm (Fig. 5).

The relative amount of the supercontinuum energy W_{sc}/W, where W is the input pulse energy, grows along the filament ($z > z_f''$) (Fig. 11). The largest conversion efficiency of the laser radiation to spectral continuum is attained for the longer filaments, i.e focal length $f = 73.5$ mm and larger value of $F = 14.7$ (Fig. 11a–d, dashed curves). The starting point of supercontinuum generation coincides with the start of the filament $z \approx z_f''$. Following the SC energy growth for $W = 3$ μJ (panel d, $P_{peak}/P_{crit} \approx 15$), we see that for a 73.5 mm lens, the conversion of the laser energy to supercontinumm is initiated early, before the geometrical focus at $z \approx -1.3$ mm (compare Fig. 11d, dashed curve, and the fluence distribution in Fig. 10c). For a 43.1 mm lens and smaller value of $F = 8.6$, the starting point of the SC generation $z \approx -0.4$ mm is closer to the geometrical focal position (compare Fig. 11d, dash-dotted curve, and the fluence distribution in Fig. 10b). For the tight focusing with $f = 16.9$ mm ($F = 3.4$), the spectral broadening starts only at $z \approx -0.1$ mm (compare Fig. 11d, solid curve, and the fluence distribution in Fig. 10a). For a constant geometrical focal distance the relative energy contained in the supercontinuum increases with an increase in the input pulse energy. This may be seen by following the increase of the maximum value of the SC energy obtained with $f = 16.9$ mm (Fig. 11a–d, solid curves) or $f = 43.1$ mm (Fig. 11a–d, dash-dotted curves) focal length lenses.

The generation of the supercontinuum is the result of self-phase modulation of the light field [34] and self-steepening [14, 15] under the conditions of strong nonlinear optical interaction with the medium. Transverse distributions of the laser intensity in the leading and trailing parts of a 3 μJ pulse ($P_{peak}/P_{crit} \approx 15$) are shown in Fig. 12 for three different focal lengths: (a) $f = 16.9$ mm, $F = 3.4$, (b) $f = 43.1$ mm, $F = 8.6$ and (c) $f = 73.5$ mm, $F = 14.7$. In the front of the pulse, the intensity maximum is on the beam axis (Fig. 12a–c, dashed curves). The time scale of this maximum is on the

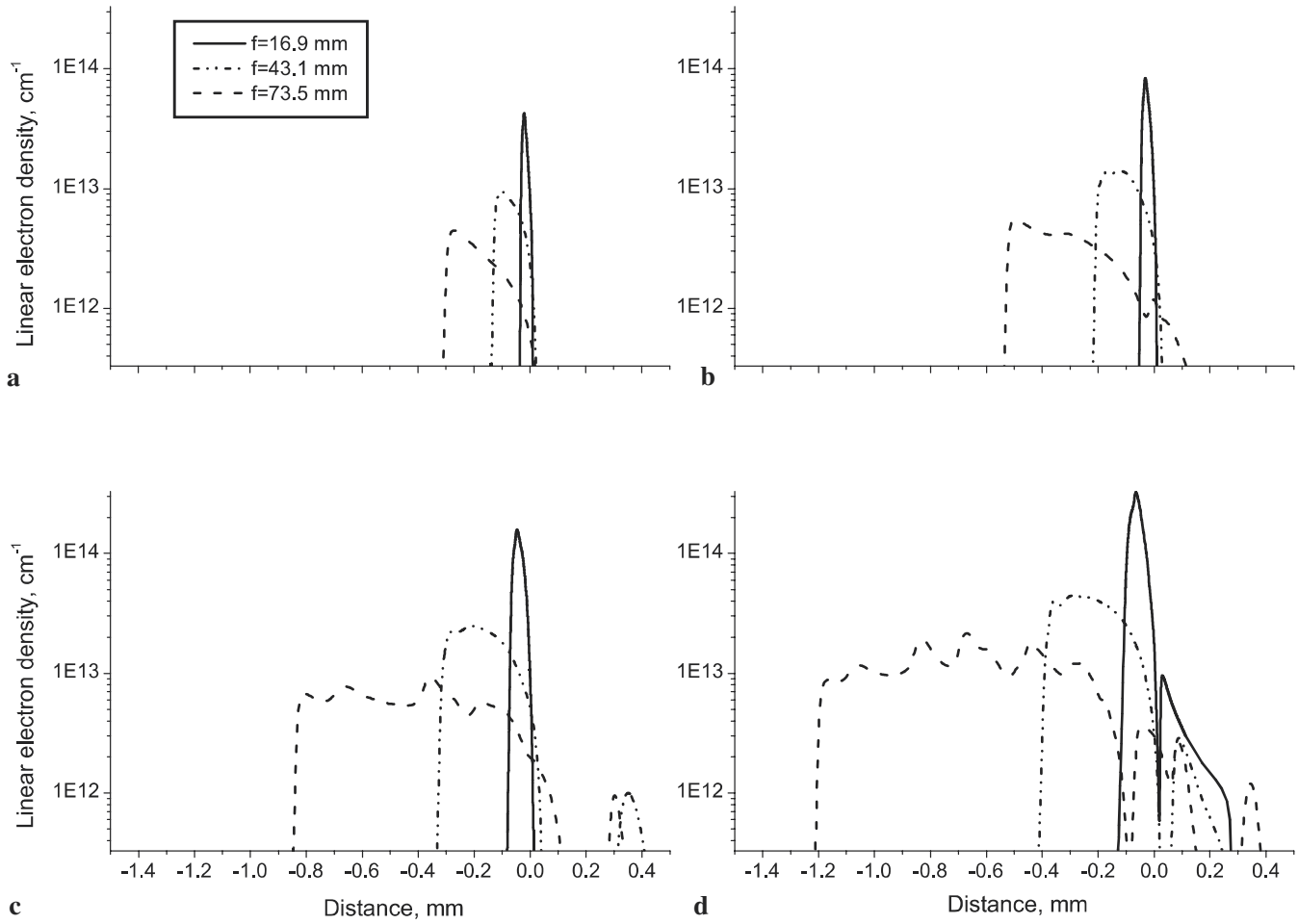

FIGURE 13 The simulated linear electron density given by (14) as a function of the propagation distance. The position of the geometrical focus is at $z = 0.0$ mm. The *solid curve* corresponds to a $f = 16.9$ mm focal distance, $F = 3.4$, the *dash-dotted curve* corresponds to a $f = 43.1$ mm focal distance, $F = 8.6$, and the *dashed curve* corresponds to a $f = 73.5$ mm focal distance, $F = 14.7$. The initial pulse energies are: **a** 0.2 μJ, $P_{\text{peak}}/P_{\text{crit}} = 1.01$; **b** 0.4 μJ, $P_{\text{peak}}/P_{\text{crit}} \approx 2$; **c** 1 μJ, $P_{\text{peak}}/P_{\text{crit}} \approx 5$; **d** 3 μJ, $P_{\text{peak}}/P_{\text{crit}} \approx 15$. The results for $W = 3$ μJ, $f = 16.9$ mm were obtained with self-steepening in (7) taken into consideration

order of 5 fs. The electron density accumulated during this time is high enough to strongly defocus the trailing part of the pulse (Fig. 12a–c, solid curves). The ring structure created at the back of the pulse essentially contributes to the generation of the SC [43]. These rings have been predicted in various theoretical papers [44, 45] and have been observed by us in air [46]. Since the temporal size of the high intensity peak in the front of the pulse is much smaller than the pulse duration, the amount of energy in this peak is also small. This is in accordance with the black area in the fluence distribution of Fig. 10a–c. There, the fluence distribution has a dip at $r = 0$. The major part of the input pulse energy is pulled off the axis due to the severe divergence. Both the rings and the dip in the fluence distribution are very well pronounced at 43.1 mm and 73.5 mm focal distances ($F = 8.6$ and 14.7, respectively). The dip is seen in the form of a dark strip on the axis (Fig. 10a–c) and the rings are seen in the form of white strips (Fig. 10b, c). If the focal distance decreases to $f = 16.9$ mm ($F = 3.4$) a strong convergence of the beam as a whole towards the geometrical focus takes place. The rings in this case are narrower than for $f = 43.1$ mm and $f = 73.5$ mm (compare Fig. 12a and c, solid curves) and they can hardly be seen within a bright sickle-shaped fluence structure (Fig. 10a and the inset in it). The diameter of the inner intensity ring in the trailing part of the pulse characterizes the transverse size of the region in which the nonlinear phase growth is the strongest. This spatio-temporal phase growth leads simultaneously to the ring formation and generation of the supercontinuum. For a short focal length lens, the propagation distance, along which this nonlinear phase growth exists, is shorter. For a lens with a longer focal length, this propagation distance is longer, the white strips indicating the rings in the fluence distribution persist for a longer distance (Fig. 10b and c). Therefore, the energy accumulated in the supercontinuum by the position of the geometrical focus is larger in the case of a long focal length lens (Fig. 11a–d, dashed curves).

3.3 *Comparison of simulation and experimental results*

In order to correlate the experimentally obtained breakdown signal on PD2 and the simulated plasma distribution, we have integrated the free electron density shown in Figs. 8–10 over the transverse coordinates. At the end of the pulse and for each position along the propagation axis we obtained the value further referred to as the linear electron

density:

$$D_e(z) = 2\pi \int_0^\infty N_e(r, z) r dr. \quad (14)$$

The quantity D_e is the total number of electrons per unit length along the propagation axis z. The results of the numerical simulations are plotted in Fig. 13 for different pulse energies (panels a to d) and focal lengths (line styles, see legend). Along with the linear electron density D_e we show the conventional electron density N_e in the absolute units of cm^{-3}, as well as the one normalized to the density of neutrals N_a (Fig. 14b). Both the linear electron density D_e and the conventional density N_e follow the maxima and the minima in the dependence of the peak pulse intensity (Fig. 14a). The highest intensity value reached in the simulations is within the interval $4 \times 10^{13} \sim 5 \times 10^{13}$ W/cm^2 and varies slightly depending on the geometrical focal distance. A further intensity increase is not possible due to the nonlinear defocusing in the laser-produced plasma. The highest possible intensity reached due to self-focusing can only be found from the test calculations for the collimated beam ($f = \infty$). These test calculations give a maximum intensity of 4.4×10^{13} W/cm^2, which is in good agreement with the highest intensity obtained for the focusing geometry.

The value of N_e in Fig. 14b represents only the local information on the on-axis plasma density. The maximum of N_e changes by 2–3 times in going from a short geometrical focal length $f = 16.9$ mm to long geometrical focal length $f = 73.5$ mm. The maximum of the linear density D_e, calculated for different geometrical focal distances, changes more than an order of magnitude and characterizes the total distribution of the plasma in the focal volume (compare Figs. 13d and 14b). The scattered light signal detected by PD2 is defined by the maximum value of the linear electron density D_e. The growth of the maximum value of D_e with input pulse energy for different geometrical focal distances is shown in Fig. 15. As a threshold breakdown density $D_{e\,th}$ we can consider the value of $D_{e\,th}$ to be 10^{13} cm^{-1}. Indeed, this is the maximum value that is achieved for the case of a 0.4 μJ ($P_{peak}/P_{crit} \approx 2$) energy in the input pulse and the geometrical focal distance $f = 43.1$ mm ($F = 8.6$) (see horizontal line in Fig. 15). According to Fig. 2, the combination of this geometrical focal length and energy gives us the optical breakdown threshold. We can verify the chosen threshold by comparing the maximum linear densities for other energies and focal lengths with the value of $D_{e\,th}$.

The values of D_e lying above the horizontal line in Fig. 15 indicate the combination of parameters for which optical breakdown should be observed according to our definition of $D_{e\,th}$. This is in agreement with the experimentally observed breakdown thresholds shown in Fig. 2 by empty squares. For example, the value of D_e for $W = 0.2$ μJ and $f = 43.1$ mm ($P_{peak}/P_{crit} = 1.01$, $F = 8.6$) is slightly below the threshold, while the value of D_e for $W = 3$ μJ ($P_{peak}/P_{crit} \approx 15$) and all focal distances considered is well above the threshold. Thus, the simulated breakdown plasma qualitatively corresponds to the experimental one. The only point in Fig. 15 that does not quite agree is the combination of the input pulse energy of 1 μJ and the focal length of 73.5 mm ($P_{peak}/P_{crit} \approx 5$, $F = 14.7$).

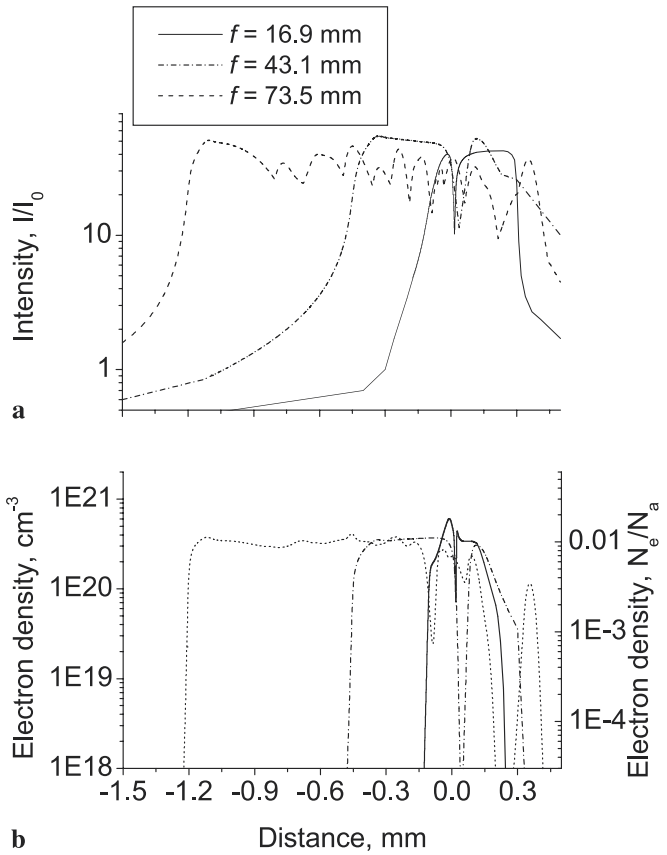

FIGURE 14 **a** The maximum intensity on the beam axis ($r = 0$) and **b** the simulated maximum electron density N_e as functions of the propagation distance inside the water cell. The position of the geometrical focus is at $z = 0.0$ mm. The *solid curve* corresponds to a $f = 16.9$ mm focal distance ($F = 3.4$), the *dash-dotted curve* corresponds to a $f = 43.1$ mm focal distance ($F = 8.6$), and the *dashed curve* corresponds to a $f = 73.5$ mm focal distance ($F = 14.7$). The initial pulse energy is 3 μJ, $I_0 = 10^{13}$ W/cm^2, and $N_a = 3.3 \times 10^{22}$ cm^{-3}

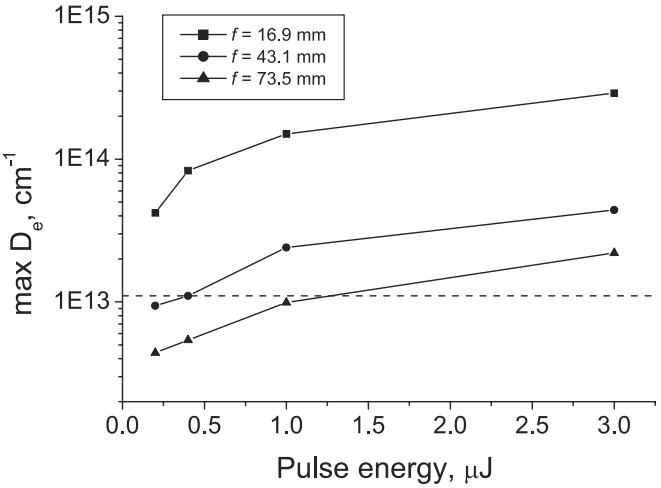

FIGURE 15 The growth of the maximum value of the linear electron density D_e with input pulse energy. *Squares*, $f = 16.9$ mm ($F = 3.4$); *circles*, $f = 43.1$ mm ($F = 8.6$); *triangles*, $f = 73.5$ ($F = 14.7$). The *dashed horizontal line* shows the threshold linear electron density $D_{e\,th}$

However, this very slight deviation is within the experimental error.

Analyzing the conversion of the radiation to the supercontinuum, we see that for the low input pulse energies of $W = 0.2\ \mu J$ and $W = 0.4\ \mu J$ ($P_{peak}/P_{crit} = 1.01$ and 2, respectively) the supercontinuum energy W_{sc} in the case of a 73.5 mm lens is much larger than the supercontinuum energy for the shorter focal lengths (compare Figs. 11a and 7a). With an increase of the input pulse energy to $W = 1\ \mu J$ (Fig. 11c, $P_{peak}/P_{crit} \approx 5$), the supercontinuum appears not only for a 73.5 mm lens, but also for a 43.1 mm lens, in agreement with the curve for the SC threshold in Fig. 2. For a high input pulse energy of $W = 3\ \mu J$ ($P_{peak}/P_{crit} \approx 15$), the supercontinuum is generated for all geometrical focal distances, including the short one of 16.9 mm (compare Figs. 7d and 11d).

Thus, in the simulations as well as in the experiment, for low pulse energies, $W < 0.4\ \mu J$ ($P_{peak}/P_{crit} < 2$), the supercontinuum is observed only for a long focal length lens, $f = 73.5$ mm ($F = 14.7$), while breakdown is observed only for a tightly focused pulse with $f < 43.1$ mm ($F < 8.6$). For intermediate pulse energies, $W \approx 1\ \mu J$, the breakdown and supercontinuum coexist for $f \geq 43.1$ mm. For high energies, $W \approx 3\ \mu J$, both supercontinuum and optical breakdown are observed for all geometrical focal distances f considered.

The simulations for a geometrical focal length of $f = 16.9$ mm were performed with the self-steepening terms in (7) taken into consideration. The comparison of the numerical results obtained for the short geometrical focal length with and without self-steepening show that there is a decrease in the supercontinuum energy in the presence self-steepening. This decrease takes place because the inclusion of the operator $\frac{i}{\omega}\frac{\partial}{\partial\tau}$ in (7) results in the smoothing of the leading front of the pulse and a decrease in the temporal phase gradients, which, in turn, causes smaller broadening of the blue wing. In particular, at an energy of $W = 3\ \mu J$ and focal length of $f = 16.9$ mm, the supercontinuum energy shows a 50% decrease in comparison with the simulation results obtained without self-steepening.

We expect that for large geometrical focal length such as $f = 73.5$ mm, the self-steepening will lead to an increase in the supercontinuum energy W_{sc}, due to the formation of multiple intensity spikes with steep leading and trailing edges in the pulse intensity distribution.

Our simulation results presented in Figs. 2, 5, 8–15 are in qualitative agreement with the experiment. Steps towards a quantitative comparison between the simulated and experimental results include, in addition to the consideration of self-steepening, an adequate description of the wide background of the small scale transverse structure of the radiation on the beam axis created due to both self-focusing and geometrical focusing. To do this a different numerical approach should be used based on a non-equidistant grid step in the radial direction [47].

3.4 *Moving white light and multiple filamentations*

We can now explain the moving white light spot that we observed when we used the shortest focal length lens ($f = 16.9$ mm). The above simulation shows that the shorter the focal length, the stronger the OB plasma and the larger its transverse size. This plasma is very unstable and sensitive to laser fluctuations. Filamentation also co-exists and is mixed with OB, as our simulation shows. In this case, the starting point of filamentation (i.e. the self-focus) is very close to the geometrical focus where OB occurs. The propagation of the deformed pulses (white light supercontinuum) will be "blocked" (diffracted and refracted) by the OB plasma. As such, from shot to shot, the unstable OB plasma will not only destroy the balance between the Kerr self-focusing and the defocusing by the plasma, but also deviate the forward propagating white light supercontinuum in a random way. In our experiments it was manifested by the decrease of the repetition rates of the white light signal in Fig. 6c and the rare shots recorded by the CCD camera, with the appearance of the jumping behavior of the white light and the random color distribution inside the SC.

On the other hand, our simulation shows that in the case of longer focal lengths, the transverse size of the OB plasma is smaller, while the wing structure of filamentation is larger (Fig. 12). Hence, the deflection effect of the OB plasma is not obvious, as in the case of shorter focal lengths. Experimentally, we consistently observed the forward propagating white light pulse (Fig. 6a).

So far, our discussion has centered around the propagation of a Gaussian laser pulse giving rise to one filament only. Actually in our experiments it was impossible to have a perfect Gaussian beam. The nonlinear propagation is very sensitive to the spatial energy distribution [21, 48]. A non-ideal spatial energy distribution will induce the generation of multiple filaments instead of increasing the filament length if the laser energy is high enough. Previous observations have shown multiple filaments distributed like an arrowhead around the focusing cone in water [49]. We expect that the peak intensity in each of these filaments is almost constant because of intensity clamping [13]. According to Fig. 7b, c, and d, we recorded a flat around 1 mV, which indicates that there was only single filament. Also, multiple filaments are manifested in Figs. 6 and 7. In Fig. 6, the signal increases from panel b to panel a, while in Fig. 7, the detected energy changes from the 1 mV level to 10 mV and even to the level of several tens of mV. This dramatic signal change indicates that we passed from single to multiple filaments in the experiment.

We summarize our observations in Fig. 16, in which the appearance of the three stages of the filamentation process, creation of the filament and moving white light (open triangle), single filament (filled triangle) and multiple filaments (open squares), is represented as a function of the distance $\Delta f = f - z_f'$ ($\Delta f = |z_f''|$) between the self-focus and the geometrical focus (breakdown spot) and as a function of the focal length f. We identify three zones, which are limited by certain values of Δf. Zone III ($\Delta f \leq 0.25$ mm) corresponds to the stage in which the moving white light phenomenon is observed. For $0.25\ \text{mm} < \Delta f < 1$ mm (Zone II) a single stable filament is formed, while for distances of at least 1 mm between the self-focus and the geometrical focus (Zone I) multiple filamentation occurs. This allows us to estimate the maximum "cone length" of the breakdown spot to be smaller than 0.25 mm from the geometrical focus, since as soon as the self-focus moves further away from the geometrical focus, the moving white light phenomenon disappears and a stable filament is observed. Furthermore, the maximum filament length

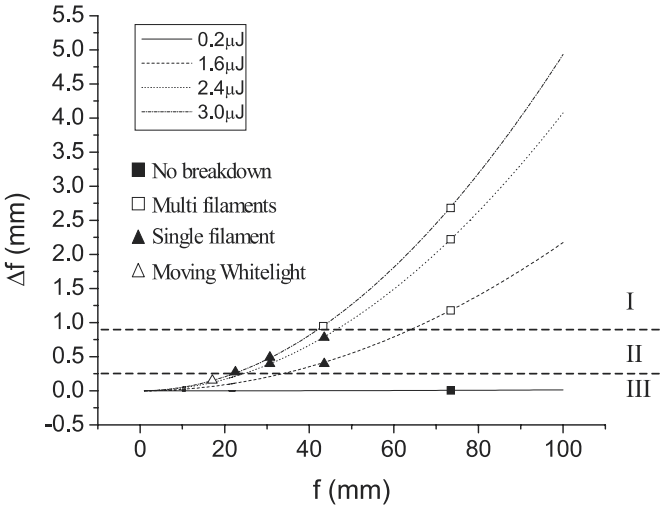

FIGURE 16 Different filamentation stages as functions of the geometrical focal length f and of the distance between the self-focus and geometrical focus Δf

can be estimated to be about 0.5 to 1 mm before multiple filaments occur.

4 Conclusion

We have investigated, both experimentally and numerically, the joint manifestation of self-focusing, filamentation, optical breakdown and supercontinuum generation in the course of focusing of femtosecond laser pulses in water, an example of condensed matter. It is shown that the coexisting states of OB and SC mainly depend on the geometrical focal conditions. For long focal lengths, supercontinuum generation can precede optical breakdown and for shorter focal lengths, both phenomena can coexist together in the optical medium. If the focal length is short enough, optical breakdown will precede supercontinuum generation. The filamentation process is characterized, from its creation near the geometrical focus, by the formation of a stable single filament to the formation of multiple filaments, as a function of the distance between the self-focus and the breakdown spot. We observed the appearance of a randomly distributed white light beam as a characteristic signature of the appearance of filamentation and supercontinuum generation near the breakdown plasma.

ACKNOWLEDGEMENTS This work has been partially supported by NATO, NSERC, DREV, le Fonds FCAR, CIPI, Canada Research Chairs, the Alexander von Humboldt-Foundation, DFG and the Russian Fund for Basic Research 00-02-17497.

REFERENCES

1 K.M. Davis, K. Miura, N. Sugimoto, K. Hirao: Opt. Lett. **21**, 1729 (1996)
2 K. Hirao, K. Miura: J. Non-Cryst. Solids **239**, 91 (1998)
3 L. Sudrie, M. Franco, B. Prade, A. Mysyrowicz: Opt. Commun. **191**, 333 (2001)
4 K. Yamada, W. Watanabe, T. Toma, K. Itoh, J. Nishii: Opt. Lett. **26**, 19 (2001)
5 E. Yablonovitch, N. Bloembergen: Phys. Rev. Lett. **29**, 907 (1972)
6 W. Lee Smith, P. Liu, N. Bloembergen: Phys. Rev. A **15**, 2396 (1977)
7 P.B. Corkum, C. Rolland, T. Srinivasan-Rao: Phys. Rev. Lett. **57**, 2268 (1986)
8 A. Braun, G. Korn, X. Liu, D. Du, J. Squier, G. Mourou: Opt. Lett. **20**, 73 (1995)
9 L. Wöste, C. Wedekind, H. Wille, P. Rairoux, B. Stein, S. Nikolov, C. Werner, S. Niedermeier, F. Ronneberger, H. Schillinger, R. Sauerbrey: Laser Optoelektronik **29**, 51 (1997)
10 A. Brodeur, S.L. Chin: Phys. Rev. Lett. **80**, 4406 (1998)
11 A. Brodeur, S.L. Chin: J. Opt. Soc. Am. B **16**, 637 (1999)
12 R. Rairoux, H. Schillinger, S. Niedermeier, M. Rodriguez, F. Ronneberger, R. Sauerbrey, B. Stein, D. Waite, C. Wedekind, H. Wille, L. Wöste, C. Ziener: Appl. Phys. B **71**, 573 (2000)
13 W. Liu, S. Petit, A. Becker, N. Aközbek, C.M. Bowden, S.L. Chin: Opt. Commun. **202**, 189 (2002)
14 N. Aközbek, M. Scalora, C.M. Bowden, S.L. Chin: Opt. Commun. **191**, 353 (2001)
15 A.L. Gaeta: Phys. Rev. Lett. **84**, 3582 (2000)
16 R.R. Alfano (Ed.): *The Supercontinuum Laser Source* (Springer, New York 1989)
17 S.L. Chin, A. Brodeur, S. Petit, O.G. Kosareva, V.P. Kandidov: J. Nonlinear Opt. Phys. Mater. **8**, 121 (1999)
18 S.L. Chin, K. Miyazaki: Jpn. J. Appl. Phys. **38**, 2011 (1999)
19 X.M. Zhao, J.-C. Diels, C.V. Wang, J.M. Elizondo: IEEE J. Quantum Electron. **QE-31**, 599 (1995)
20 K.R. Wilson, V.V. Yakovlev: J. Opt. Soc. Am. B **14**, 444 (1997)
21 H. Schillinger, R. Sauerbrey: Appl. Phys. B **68**, 753 (1999)
22 A. Talebpour, M. Abdel-Fattah, S.L. Chin: Opt. Commun. **183**, 479 (2000)
23 J. Kasparian, R. Sauerbrey, S.L. Chin: Appl. Phys. B **71**, 877 (2000)
24 A. Becker, N. Aközbek, K. Vijayalakshmi, E. Oral, C.M. Bowden, S.L. Chin: Appl. Phys. B **73**, 287 (2001)
25 H.R. Lange, A. Chiron, J.F. Ripoche, A. Mysyrowicz, P. Breger, P. Agostini: Phys. Rev. Lett. **81**, 1611 (1998)
26 F.A. Ilkov, L.S. Ilkova, S.L. Chin: Opt. Lett. **18**, 681 (1993)
27 J.H. Marburger: Prog. Quantum Electron. **4**, 35 (1975)
28 D.W. Fradin, N. Bloembergen, J.P. Latellier: Appl. Phys. Lett. **22**, 636 (1973)
29 V. François, F.A. Ilkov, S.L. Chin: J. Phys. B. **25**, 2709 (1992)
30 Y.P. Raizer: *Gas Discharge Physics* (Springer-Verlag, New York 1991)
31 P.K. Kennedy, S.A. Boppart, D.X. Hammer, B.A. Rockwell, G.D. Noojin, W.P. Roach: IEEE J. Quantum Electron. **QE-31**, 2250 (1995)
32 D. Du, X. Liu, G. Korn, J. Squier, G. Mourou: Appl. Phys. Lett. **64**, 3071 (1994)
33 Q. Feng, J.V. Moloney, A.C. Newell, E.M. Wright, K. Cook, P.K. Kennedy, D.X. Hammer, B.A. Rockwell, C.R. Thompson: IEEE J. Quantum Electron. **QE-33**, 127 (1997)
34 I.S. Golubtsov, V.P. Kandidov, O.G. Kosareva: Atmos. Oceanic. Opt. **14**, 303 (2001)
35 T. Brabec, F. Krausz: Phys. Rev. Lett. **78**, 3282 (1997)
36 S.L. Chin, S. Petit, W. Liu, A. Iwasaki, M.-C. Nadeau, V.P. Kandidov, O.G. Kosareva, K.Y. Andrianov: Opt. Commun. **210**, 329 (2002)
37 A.M. Perelemov, V.S. Popov, M.V. Terent'ev: Sov. Phys. JETP **23**, 924 (1966)
38 I.K. Kikoin (Ed.): *Tablitsy Fizicheskikh Velichin. Spravochnik (Tables of Physical Values)* (Atomizdat, Moscow 1976)
39 A. Maitland, M.H. Dunn: *Laser Physics* (North-Holland, Amsterdam 1969)
40 S. Tzortzakis, L. Sudrie, M. Franco, B. Prade, A. Mysyrowiez: Phys. Rev. Lett. **87**, 213 902 (2001)
41 A. Talebpour, S. Petit, S.L. Chin: Opt. Commun. **129**, 285 (1999)
42 N. Aközbek, C.M. Bowden, A. Talebpour, S.L. Chin: Phys. Rev. E **61**, 4540 (2000)
43 O.G. Kosareva, V.P. Kandidov, A. Brodeur, S.L. Chin: J. Nonlinear Opt. Phys. Mater. **6**, 485 (1997)
44 S.C. Rae: Opt. Commun. **104**, 330 (1994)
45 V.P. Kandidov, O.G. Kosareva, S.A. Shlenov: Quantum Electron. **24**, 905 (1994)
46 S.L. Chin, N. Aközbek, A. Proulx, S. Petit, C.M. Bowden: Opt. Commun. **188**, 181 (2001)
47 O. G Kosareva, V.P. Kandidov, A.A. Koltun, S.L. Chin: In: *Technical Digest of Int. Quantum Electron. Conf. in Moscow, 22–27 June 2002*, p. 196
48 M. Mlejnek, M. Kolesik, J.V. Moloney, E.M. Wright: Phys. Rev. Lett. **83**, 2938 (1999)
49 A. Brodeur, F.A. Ilkov, S.L. Chin: Opt. Commun. **171**, 193 (1996)